physica status solidi pss rrl
www.pss-rapid.com

Sputter-Grown $MnBi_2Te_4$ Thin Films: Magnetic Ground States and Phase Control

*Joshua Bibby, Emily Heppell, Jack Bollard, Ethan L. Arnold, Javier Herrero-Martín, Gerrit van der Laan, and Thorsten Hesjedal**

The synthesis and magnetic properties of the intrinsic magnetic topological insulator $MnBi_2Te_4$, grown by magnetron sputtering, are investigated. While this growth method enables smoother morphologies than molecular beam epitaxy and is compatible with scalable processing, the metastable nature of $MnBi_2Te_4$ presents considerable challenges in phase control and magnetic uniformity. By systematically varying the relative sputter powers of Mn, Bi_2Te_3, and Te targets, conditions that favor the formation of near-stoichiometric $MnBi_2Te_4$, as supported by X-ray diffraction, atomic force microscopy, and energy-dispersive X-ray spectroscopy, are identified. These films exhibit reduce surface roughness and lower twin-domain density compared to Mn-rich counterparts, which show evidence of phase separation and structural disorder. Magnetometry and X-ray magnetic circular dichroism reveal that both film types exhibit sizable Mn moments, although signatures of antiferromagnetic order are only weakly expressed and appear sensitive to composition and morphology. Despite producing structurally well-ordered films, clear linear dichroism attributable to A-type antiferromagnetic ordering is not observed, suggesting magnetic inhomogeneity or suppression of interlayer coupling. These results highlight the compositional sensitivity of sputtered $MnBi_2Te_4$ and underline the difficulties in stabilizing the intrinsic magnetic topological phase in thin-film form.

1. Introduction

Topological insulators (TIs) have emerged as a new class of quantum materials with potential for dissipationless and spin-polarized surface transport.[1] In these systems, strong spin-orbit coupling and time-reversal symmetry protection lead to spin-momentum-locked surface states that are robust against non-magnetic scattering.[2] TIs in two dimensions can be understood as time-reversed counterparts of the quantum Hall effect, effectively realized by two copies of the Haldane model with opposite spin, while their 3D counterparts represent a bulk generalization of this quantum spin Hall state.[2] When interfaced with magnetic layers or directly doped, these materials offer a platform to realize novel quantum phases such as the quantum anomalous Hall effect (QAHE), axion insulators, or Majorana edge states.[3]

Despite progress in tuning topological surface transport via doping and gating, many challenges remain. In binary chalcogenides such as Bi_2Te_3 and Bi_2Se_3, bulk conduction from native defects[4] often dominates over surface transport,[5,6] and attempts to reduce this via counter-doping or alloying[7,8] often lead to diminished mobility and structural disorder.[9] Magnetic doping[10] has shown promise in breaking time-reversal symmetry, enabling access to Chern insulator phases with dissipationless edge conduction.[11] However, transition metal doping often results in inhomogeneous phase formation, magnetic clustering, or poor reproducibility at higher dopant levels.[12,13]

The compound $MnBi_2Te_4$ (MBT) offers a compelling alternative, as it incorporates Mn atoms directly into the crystal lattice, forming an intrinsic magnetic TI.[14–20] MBT consists of septuple layers (SLs) composed of Te-Bi-Te-Mn-Te-Bi-Te stacking, with ferromagnetic ordering within each SL and antiferromagnetic coupling between SLs. This A-type antiferromagnetic structure

J. Bibby, E. Heppell, J. Bollard, E. L. Arnold, T. Hesjedal
Department of Physics
University of Oxford
Parks Road, Oxford OX1 3PU, UK
E-mail: t.hesjedal1@physics.ox.ac.UK

The ORCID identification number(s) for the author(s) of this article can be found under https://doi.org/10.1002/pssr.202500329.

DOI: 10.1002/pssr.202500329

E. Heppell, J. Bollard, E. L. Arnold, G. van der Laan, T. Hesjedal
Diamond Light Source
Harwell Science and Innovation Campus
Didcot OX11 0DE, UK

E. Heppell
ISIS
Rutherford Appleton Laboratory
Harwell Science and Innovation Campus
Didcot OX11 0QX, UK

J. Herrero-Martín
ALBA Synchrotron
Carrer de la Llum 2-26, 08290 Cerdanyola del Vallès, Barcelona, Spain

makes MBT the first example of an intrinsic magnetic TI.[15,21] MBT supports time-reversal symmetry breaking and hosts a variety of topological phases depending on the number of SLs and stacking configurations.[22,23] For an odd number of layers, a net uncompensated magnetization supports the QAHE,[24,25] whereas an even number yields a zero Hall plateau consistent with the axion insulator state.[23,24,26] Moreover, recent studies have linked MBT heterostructures to platforms for realizing Majorana fermions via topological superconductivity.[27]

These discoveries have renewed interest in Mn-doped Bi_2Te_3 systems, where varying Mn content leads to magnetic transitions, secondary phase formation, and transport anomalies.[12,13] Our previous work demonstrated that Mn doping of Bi_2Te_3 via magnetron sputtering leads to grain-size-tunable films but suffers from phase inhomogeneity and limited magnetic coherence at high Mn concentrations.[13] At sufficiently high Mn content, spontaneous formation of the MBT phase was observed, offering a route to stabilizing magnetic topological order in sputtered films.

MBT thin films have primarily been grown by molecular beam epitaxy (MBE), which enables atomically precise layer control. However, MBE-grown MBT films have so far failed to exhibit the key phenomena predicted for intrinsic magnetic TIs. Despite their high structural quality, no experimental reports have conclusively demonstrated QAHE or axion insulating behavior in such films, with all high-quality data to date obtained from exfoliated single crystals. Additionally, the step-flow morphology and surface roughness inherent to MBE growth complicate element-specific spectroscopy, such as X-ray magnetic circular and linear dichroism (XMCD/XMLD), as surface inhomogeneity averages out the signal from alternating magnetic layers.[22,28–34]

Magnetron sputtering, in contrast, offers a scalable, CMOS-compatible deposition technique capable of smoother film morphologies through kinetic energy tuning and post-growth annealing.[35] Our original aim was to exploit this growth mode to stabilize MBT with sufficiently low roughness to enable clear observation of even–odd XMLD signatures associated with the layered antiferromagnetic structure. While Lu et al.[35] have demonstrated sputtered MBT exhibiting antiferromagnetic order and spin-flop transitions, detailed phase analysis and element-specific magnetic studies remain lacking. Moreover, in our own experiments, no trustworthy XMLD signal could be extracted, even from the smoothest films, suggesting significant local magnetic disorder or suppression of interlayer coupling.

In this work, we investigate the structural and magnetic properties of MBT thin films grown by magnetron sputtering. We explore the role of sputter power ratios in determining phase purity and magnetic response, and we identify regimes where MBT forms stoichiometrically and exhibits coherent magnetic order. Using X-ray diffraction (XRD), atomic force microscopy (AFM), and energy-dispersive X-ray spectroscopy (EDS) in an scanning electron microscope (SEM), we assess crystallinity and morphology. Magnetic properties are investigated via superconducting quantum interference device vibrating sample magnetometer (SQUID-VSM) magnetometry, complemented by element-specific X-ray absorption spectroscopy (XAS) and X-ray magnetic circular dichroism (XMCD) at the Mn $L_{2,3}$ edges. Our results establish magnetron sputtering as a viable route for synthesizing MBT thin films and provide key insight into the growth–composition–magnetism relationship in this promising class of materials.

2. Results and Discussion

2.1. Thin Film Growth and Composition

A series of MBT thin films were synthesized by magnetron sputtering with systematically varied Bi_2Te_3, Mn, and Te fluxes to tune stoichiometry and assess phase stability. **Table 1** summarizes the sputter power settings and resulting atomic compositions, determined by SEM-EDS. Throughout this work, we compare two representative samples: a stoichiometric MBT film (hereafter sMBT) and a Mn-rich variant (eMBT). Both were grown using the same cosputtering and post-annealing procedure described in Section 2, with the only distinction being the relative sputter powers applied to the Mn and Te targets, as summarized in Table 1. The sMBT film corresponds to conditions that yield a near-nominal Mn:Bi:Te stoichiometry (≈1:2:4), while the eMBT film is produced with a higher Mn flux, leading to an Mn concentration exceeding 30 at %. Both films were annealed under identical conditions (375 °C, 3 h) to ensure comparable crystallization.

A clear nonlinearity is observed between the Mn sputter power and resulting Mn concentration, particularly in response to the Te power. For instance, increasing the Te power from 5 to 8 W while keeping Mn at 4 W results in a net increase in Mn content, despite constant Mn flux. This suggests that the Mn incorporation is not determined solely by the target power but is mediated by excess chalcogen, possibly through phase stabilization or suppression of competing phases such as $MnTe_x$.

We will show below that films with Mn concentrations above 20 at.% (atomic-%) display markedly different crystallographic structures compared to those near stoichiometry, indicating a threshold beyond which the MBT phase destabilizes or phase separation occurs. These trends are consistent with earlier observations in Mn-doped Bi_2Te_3 systems, where excess Mn is known to cluster or form secondary phases rather than incorporating uniformly into the lattice.[13]

Table 1. Sputter power settings, P, and elemental compositions of selected ≈12-nm-thick MBT films, determined by SEM-EDS. Two representative samples, eMBT (Mn-rich) and sMBT (stoichiometric), are highlighted and analyzed in detail. A nonlinear dependence of Mn incorporation on sputter power is observed, with Te flux modulating Mn uptake.

Sample	$P_{Bi_2Te_3}$ [W]	P_{Te} [W]	P_{Mn} [W]	Bi (at. %)	Te (at. %)	Mn (at. %)
576 (eMBT)	20	5	10	18.7	49.2	32.2
586 (sMBT)	20	5	4	36.5	50.0	13.5
589	20	8	4	34.5	51.8	13.6
593	20	8	4	32.5	52.2	15.3

2.2. Structural Characterization

The structural properties of the MBT films were characterized by XRD using both symmetric θ–2θ scans and asymmetric RSM, shown in **Figure 1** and **Figure 2**, respectively. Symmetric scans reveal well-defined (003l) peaks in both samples, consistent with c-axis-oriented layered structures. The main (009) reflections occur near 20°, with the calculated c-lattice parameters exceeding the bulk value of 40.9 Å in both cases: 41.6 Å for the Mn-rich eMBT film and 42.4 Å for the stoichiometric sMBT film. The expanded interlayer spacing is attributed to epitaxial strain from the sapphire substrate and possible Mn intercalation in the van der Waals gap.

Although the peak positions suggest a layered phase, the proximity of the (003l) reflections in Bi_2Te_3 and MBT makes phase separation difficult to distinguish in symmetric geometry alone. As shown in Figure 2, asymmetric RSM provides additional insight: the Mn-rich sample (Figure 2a) exhibits reflections consistent with a Bi_2Te_3-like phase, while the stoichiometric film (Figure 2b) displays features attributable to MBT. This contrast suggests that excess Mn may inhibit the formation of the septuple-layer MBT phase, potentially through competition with $MnTe_x$-type secondary phases or amorphous clustering. Interestingly, despite previous observations that high Mn content can suppress Bi_2Te_3 formation,[13] our results indicate that the sputtering pathway allows Mn incorporation into non-MBT configurations beyond a threshold concentration.

To assess the in-plane domain orientation and detect stacking faults, azimuthal (φ) scans were performed on asymmetric reflections, as shown in Figure 1b. The Mn-rich film shows sixfold rotational symmetry, consistent with significant twinning, whereas the sMBT film shows the expected threefold symmetry of the rhombohedral MBT structure. Twinning in van der Waals materials is a common consequence of weak interlayer bonding and substrate symmetry mismatch,[36] and is often exacerbated during nucleation. That it is absent in the stoichiometric film suggests that the annealing step promotes domain coalescence and ordered stacking when the composition is optimal.

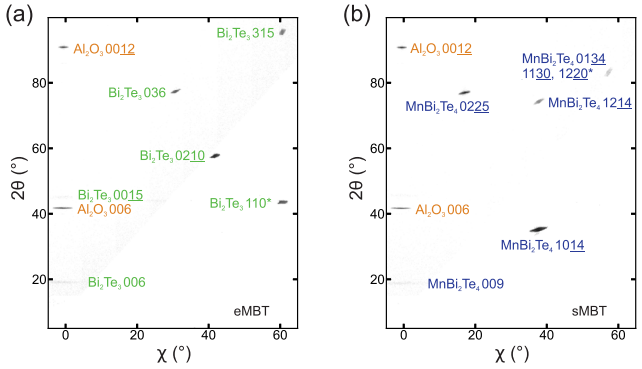

Figure 2. Asymmetric reciprocal space maps of the same films shown in Figure 1. a) The excess-Mn sample (eMBT) shows features matching Bi_2Te_3, suggesting incomplete formation of the septuple-layer structure. b) The stoichiometric sample (sMBT) displays well-defined reflections corresponding to MBT, confirming the successful stabilization of the desired phase. Peak indices denoted with an asterisk (*) are best-effort estimates based on the expected symmetry and lattice parameters.

The surface morphology and grain structure were characterized by tapping-mode AFM, shown in **Figure 3**. The Mn-rich film displays large, round grains with an average diameter of 160 nm and high surface roughness (5.6 nm). In contrast, the stoichiometric film exhibits more irregular grain shapes and substantially reduced roughness (1.3 nm), indicative of improved film uniformity. The difference in morphology is consistent with the enhanced crystallographic coherence and lower degree of twinning observed in the sMBT sample. While the average grain size in the stoichiometric sample could not be reliably extracted using watershed-based segmentation, line profile analysis yielded an estimated lateral feature spacing of ≈115 nm.

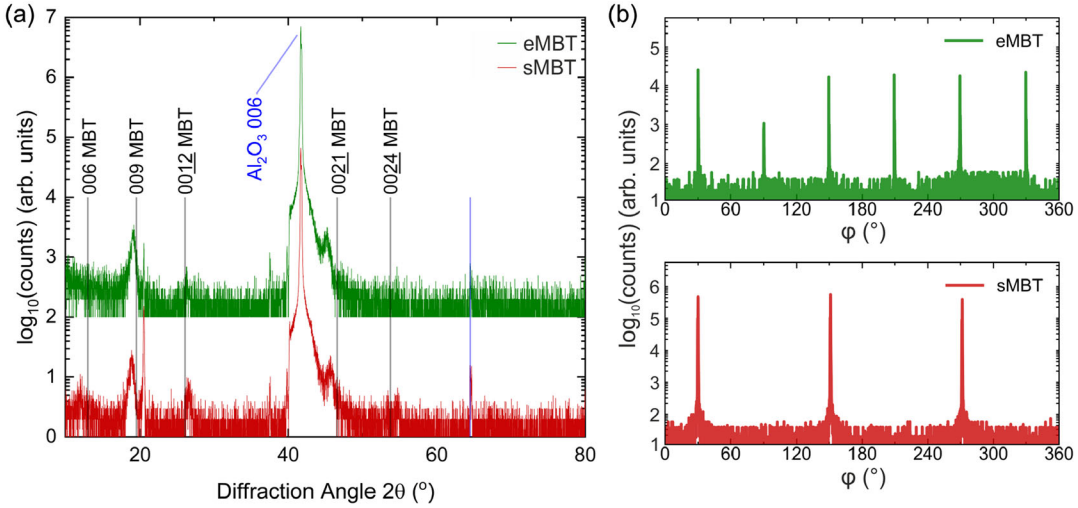

Figure 1. a) XRD patterns for the two eMBT and sMBT films grown on c-plane sapphire. Both exhibit pronounced (003l) peaks consistent with the layered structure. The peak shifts are attributed to lattice strain from substrate mismatch. b) Azimuthal φ-scans for the (036) Bi_2Te_3 and (0225) MBT reflections, showing sixfold symmetry in the Mn-rich sample and threefold symmetry in the stoichiometric sample, are consistent with stacking fault (twinning) suppression.

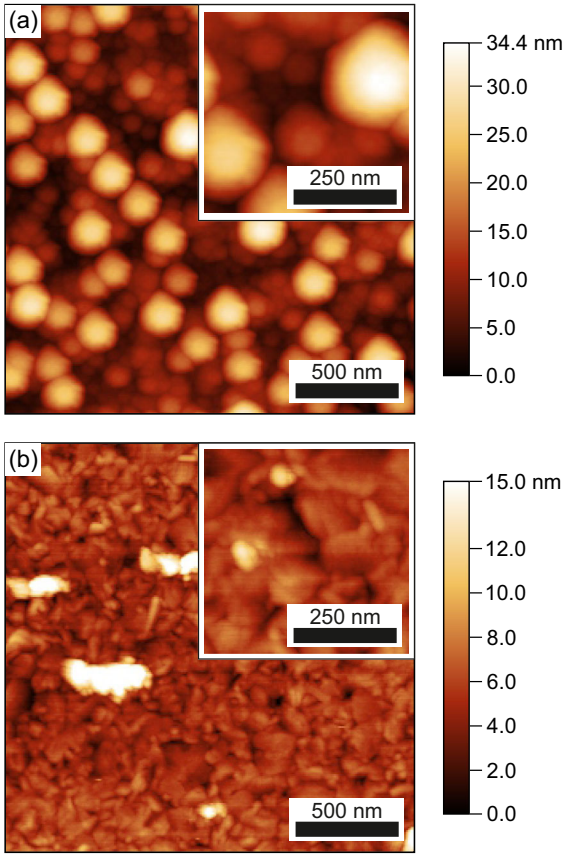

Figure 3. Tapping-mode AFM images of the eMBT and sMBT films. a) The excess-Mn film shows large, round grains (≈160 nm diameter) and high roughness (5.6 nm). b) The stoichiometric film shows more irregular grain morphology and significantly lower roughness (1.3 nm), indicative of improved surface uniformity across the sample.

The reduction in surface roughness is particularly relevant for synchrotron-based XMLD measurements, which are highly sensitive to magnetic anisotropy averaging across the beam footprint (typically on the order of 150 μm). As such, the structural improvements in the sMBT film make it a better candidate for probing layered antiferromagnetism using X-ray linear dichroism.

2.3. Magnetic Properties—Magnetometry

The magnetic properties of the films were assessed using SQUID-VSM magnetometry, with both field-dependent $[M(H)]$ and temperature-dependent $[M(T)]$ measurements shown in **Figure 4**. Out-of-plane $M(H)$ loops at 5 K (Figures 4a,b) show low coercivity and an unsaturated, near-linear magnetization behavior at high fields, characteristic of weakly coupled or paramagnetic Mn moments. Such behavior is commonly observed in Mn-doped TIs and is attributed to continuous reorientation of magnetic domains in the presence of competing ferromagnetic and antiferromagnetic interactions.[37,38] In Subsection 3.4, we present complementary XMCD hysteresis measurements using a 14 T magnet, which show a nonsaturated paramagnetic behavior, in agreement with the SQUID-VSM data.

To obtain the magnetic moments per Mn from the SQUID-VSM data, the magnetization values were first normalized by the total Mn content as determined by SEM-EDS analysis in conjunction with XRR-based film thickness measurements. Note that due to the unsaturated paramagnetic response, the weak magnetic contribution of the film, and the presence of competing paramagnetic and disordered contributions in the film, the diamagnetic subtraction using a reference substrate did not yield physical values for the magnetic moments. Therefore, in order to resolve this issue, the magnetic moment values (right-hand side axes in Figure 4a,b) were scaled to the spin moments at 5 T as determined by XMCD sum rules analysis. The sMBT film appears to approach saturation more readily in contrast to the eMBT film, indicating a more uniform magnetic environment and possibly more effective interlayer coupling, albeit still far from ideal A-type antiferromagnetism.

Temperature-dependent $M(T)$ measurements (Figure 4c,d) provide further insight into the magnetic ground states. In both films, a broad feature appears near 30–40 K, but with notable differences in character. In the eMBT film, a weak discontinuity is observed near 30 K, consistent with the onset of partial magnetic ordering. In contrast, the sMBT film displays two features: a shallow increase in moment around 35–40 K followed by a subtle anomaly near 8 K. The higher-temperature feature likely corresponds to residual interlayer coupling, while the lower-temperature kink may suggest a distinct secondary magnetic phase, such as the antiferromagnetic phase, or spin reorientation transition.

These findings support the picture of compositionally driven magnetic disorder in the eMBT film, where excess Mn may form weakly interacting ferromagnetic regions or magnetic clusters, thus elevating the moment without establishing coherent long-range order. In contrast, the sMBT film, while structurally superior, remains magnetically ambiguous, consistent with a scenario in which A-type antiferromagnetic coupling is suppressed by residual disorder or incomplete stacking coherence.

In-plane field-dependent magnetometry was also performed on the sMBT film (data not shown) but yielded a similar unsaturated response without any discernible spin-flop or anisotropic behavior. This is consistent with the absence of XMLD contrast and further supports the interpretation that robust antiferromagnetic order is not established.

2.4. Magnetic Properties—Spectroscopy

To complement bulk magnetometry and probe the magnetic behavior of Mn at the atomic level, synchrotron-based magnetic X-ray spectroscopy were performed at the Mn $L_{2,3}$ edges for both representative eMBT and sMBT films, as shown in **Figure 5**. All measurements shown were conducted in TEY mode at ≈2 K under an applied field of 6 T aligned parallel to the beam direction in normal incidence. Both samples exhibit XAS line shapes consistent with Mn^{2+} in a chalcogenide environment, with no evidence of oxidation or Mn in metallic bonding configurations.[21] The corresponding XMCD spectra reveal distinct dichroic signals in both films, indicative of net Mn magnetization. Notably, the relative size of the XMCD is larger in the Mn-rich sample, consistent with the higher total magnetization observed in SQUID measurements.

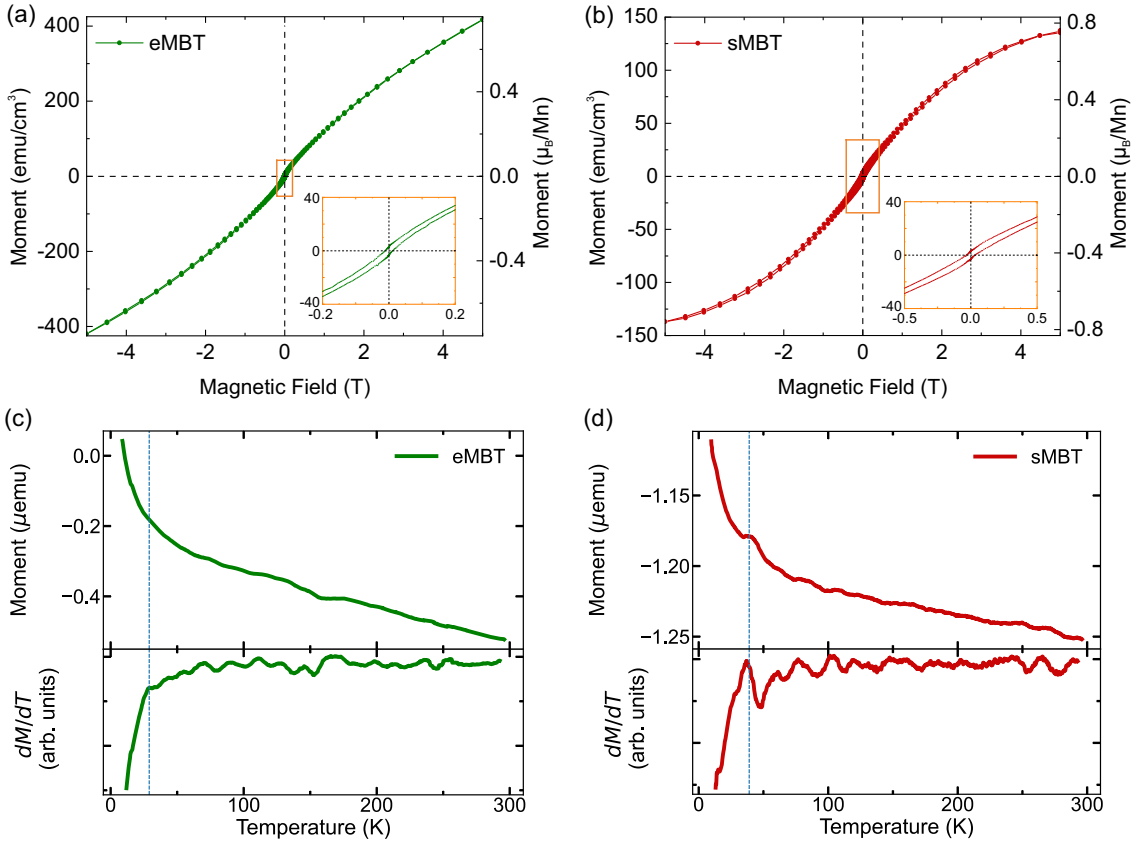

Figure 4. Field- and temperature-dependent magnetization data for both films. a,b) Field out-of-plane $M(H)$ curves at 5 K show low coercivity and paramagnetic behavior at high fields. The Mn-rich film in (a) exhibits a higher moment than the stoichiometric film (b), which, on the other hand, shows signs of saturation above 5 T. The insets highlight the low-field part of the hysteresis as indicated. c,d) $M(T)$ plots (above) measured in an out-of-plane field of 100 Oe, and their derivatives (below), reveal a weak transition near 30 K in both samples, and the sMBT film additionally shows in (d) a subtle feature at ≈8 K (both indicated by dashed vertical lines).

To extract quantitative estimates of the magnetic moments, sum rules analysis was carried out based on the normalized spectra.[39] The derived spin and orbital moments per Mn atom are $m_{spin} = 0.870\ \mu_B$ and $m_{orb} = 0.021\ \mu_B$ for eMBT, and $m_{spin} = 0.840\ \mu_B$ and $m_{orb} = 0.038\ \mu_B$ for sMBT. These values are consistent with those reported for a 16.3-nm-thick, MBE-grown MBT film.[33] (Note that the values reported in ref. [33] $m_{spin} = 1.64\ \mu_B$ and $m_{orb} = 0.16\ \mu_B$, were recorded at 3 K in a field of 14 T; the field-dependent plot of the magnetic moments shows values of ≈0.75 and <0.1 μ_B/Mn for the spin and orbital moments, respectively, at 5 T). It is worth emphasizing that these extracted moments for thin films are considerably lower than the ordered moment of ≈4 μ_B/Mn reported for bulk MBT single crystals at 10 K,[40] pointing at the existence of structural defects and/or secondary phases.[41,42]

The values derived from the sum rules give a m_{orb}/m_{spin} ratio of 0.024 and 0.045 for eMBT and sMBT, respectively. According to Hund's third rule, this means that the occupation of the 3*d* shell is slightly higher than half filled (Mn^{2+} $3d^5$), which hints at hybridization between the Mn 3*d* and Te 5*p* orbitals. The latter is further supported by the presence of the prepeak at 638.0 eV in the XMCD spectrum.[43] The marginally higher orbital moment in the sMBT film, despite its lower net magnetization, may suggest subtle differences in crystal field symmetry or Mn site occupation. However, the interpretation of this trend is complicated by the overlap of structural disorder and magnetic inhomogeneity.

Attempts were made to detect XMLD in the same films, with the goal of probing collinear A-type antiferromagnetic ordering via anisotropic absorption. Despite the improved surface smoothness and structural coherence of the sMBT sample compared to typical MBE-grown MBT films, no genuine XMLD signal could be observed under any polarization geometry or field condition. This result likely reflects a combination of residual roughness, stacking disorder, and partial magnetic decoupling between Mn layers, all of which can suppress the XMLD response by spatially averaging out uniaxial anisotropies over the beam footprint.

Figure 6 shows the XMCD hysteresis loop measured at the Mn L_3 edge in TEY mode for a compositionally and structurally similar film to the sMBT sample (sample 589; see Table 1 for details). The asymmetry, defined as $(\mu^+ - \mu^-)/(\mu^+ + \mu^-)$,[44] increases smoothly with applied field up to 14 T and exhibits no sign of magnetic saturation, consistent with paramagnetic-like behavior. This trend mirrors the magnetization response observed in the SQUID-VSM $M(H)$ data for the sMBT film shown in Figure 4b, where the moment also increases linearly without a well-defined

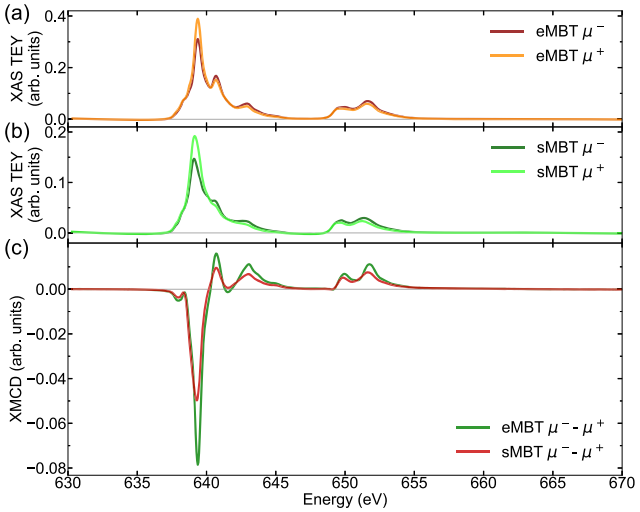

Figure 5. a,b) XAS and c) XMCD spectra measured at the Mn $L_{2,3}$ edges for MBT films with high (eMBT) and stoichiometric (sMBT) Mn content. Measurements were performed at 2 K in a 6 T out-of-plane magnetic field using TEY detection mode. (a,b) XAS under positive and negative circular polarization for the eMBT and sMBT samples, respectively. Both films exhibit similar multiplet structures characteristic of Mn^{2+} in a chalcogenide environment. (c) The larger XMCD signal in the eMBT film reflects its higher Mn moment per atom, while the overall spectral shapes suggest comparable local environments across both samples.

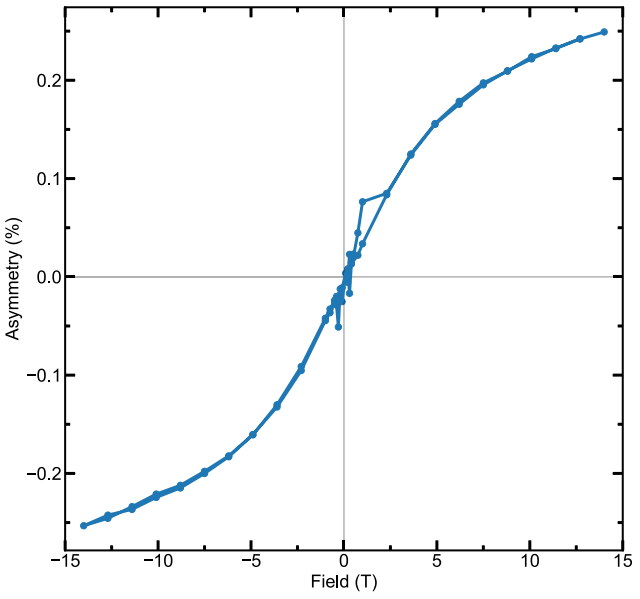

Figure 6. XMCD hysteresis loop at the Mn L_3 edge for sample 589, measured in TEY mode at ≈7.5 K. The XMCD asymmetry increases with applied field but does not saturate even at 14 T, consistent with paramagnetic-like behavior. At zero field, the TEY signal is too noisy to reliably determine the presence of residual spin polarization. Sample 589 is compositionally similar to the sMBT film.

saturation field. Although the XMCD loop appears closed, the signal-to-noise ratio near zero field is insufficient to determine whether residual spin polarization persists in the remanent state.

To evaluate whether surface-sensitive TEY data were representative of the bulk film properties, a subset of XAS measurements was performed in bulk-sensitive LY mode. While the signal-to-noise ratio was lower because the sample was much thicker than ideal for LY detection, no qualitative differences in line shape or energy position were observed, suggesting that the magnetic behavior near the surface is broadly representative of the film interior. XMCD confirms the presence of similar Mn moments in both films, and sum rules yield consistent relative moment sizes. The absence of XMLD highlights a lack of robust interlayer antiferromagnetic coupling, consistent with the ambiguous transitions observed in SQUID magnetometry and structural indications of disorder.

2.5. Discussion

The structural and magnetic properties of sputtered MBT films reveal a complex, nonlinear dependence on composition, with strong coupling between Mn content, phase stability, and magnetic ground state. While the target phase can be stabilized under near-stoichiometric conditions, deviations, especially excess Mn, lead to the emergence of parasitic phases, degraded crystallinity, and suppressed magnetic order. As indicated by both XRD and RSM, the Mn-rich film does not adopt the characteristic MBT stacking sequence and instead shows features consistent with a Bi_2Te_3-like phase. This observation contrasts with earlier studies on Mn-doped Bi_2Te_3, where increasing Mn content typically destabilizes the host lattice and suppresses the parent phase.[13] A likely reason for the discrepancy lies in the fundamental differences in synthesis methodology. In this work, films are deposited at room temperature and only crystallize during a subsequent annealing step. This approach allows for greater mobility of atoms during the anneal, which may promote phase segregation and enable the host lattice to expel excess Mn beyond what can be accommodated substitutionally or interstitially. Unlike prior work on doped Bi_2Te_3, we also include an independent Te flux during deposition, which may further stabilize Te-rich complexes or facilitate the formation of $MnTe_x$-type secondary phases. These Mn-rich regions may remain amorphous or nanocrystalline and are therefore more difficult to detect via XRD, yet they can strongly influence the film's magnetic behavior by disrupting long-range ordering or by introducing paramagnetic clusters.

The possibility of forming MnBi, a known ferromagnetic alloy,[45–47] is also consistent with our EDS data, which show a significant Bi excess and Te deficiency in the Mn-rich films. During annealing, volatile Te may desorb from the film, leading to further deviation from the ideal MBT stoichiometry and enhancing the likelihood of MnBi formation. Such secondary phases could explain the enhanced moment and paramagnetic background (MnBi in the high-temperature phase) observed in the eMBT sample, as well as the absence of any clear magnetic transition.

The sMBT film, by contrast, shows reduced roughness, minimal twinning, and structural fingerprints consistent with the MBT phase. However, the magnetic measurements reveal only weak features near 8 K and 35–40 K, and the absence of any reliable XMLD signal suggests that coherent interlayer

antiferromagnetic coupling is not achieved. Note that due to the lack of well-defined magnetic transitions, we did not carry out Curie–Weiss fits and do not state Néel temperatures. Although the XMCD-derived spin moments and the high-field $M(H)$ values normalized by Mn content are similar for both eMBT and sMBT films, this does not imply equivalent magnetic ground states. In the Mn-rich eMBT film, the excess Mn likely forms magnetically active clusters or interstitials that contribute to the total moment but do not participate in coherent interlayer coupling. These regions may behave as paramagnetic or weakly ferromagnetic inclusions, inflating the overall magnetic signal while suppressing long-range A-type antiferromagnetic order. By contrast, the sMBT film, with smoother morphology and reduced twinning, may support better stacking and magnetic coherence, though long-range disorder still prevents robust XMLD detection. The similar local Mn moment observed in both samples thus reflects preserved atomic-scale magnetism, while the differences in interlayer coupling and domain coherence define the broader magnetic behavior. We emphasize that the similar magnetization values in both samples, despite the improved structural order in sMBT, suggest that long-range magnetic coherence is more easily disrupted than local moments. If the Mn atoms in sMBT were significantly diluted or rendered magnetically inactive, one would expect a lower total moment per Mn ion, contrary to our XMCD and SQUID findings. This implies that magnetic disorder in these films likely arises from subtle disruptions in interlayer exchange pathways rather than from a loss of magnetic Mn content.

Indeed, several possible contributing factors, i.e., stacking faults, Mn intercalation into van der Waals gaps, or nonstoichiometric substitution on Bi/Te sites, have been shown to disrupt the A-type antiferromagnetic structure in epitaxial MBT.[20,22,34] In addition, excess carriers introduced by interstitial Mn or antisite defects may further destabilize the antiferromagnetic ground state.[48] In other words, although magnetron sputtering offers better surface morphology and scalable deposition, stabilizing the intrinsic magnetic topological phase of MBT in thin-film form remains a challenge. Nonetheless, the improved crystallinity and morphological control observed in our stoichiometric sputtered films, particularly the suppression of twinning and smoother surface, are encouraging signs that further refinement of growth parameters, including substrate choice and annealing conditions, could help approach the magnetic order needed for XMLD sensitivity. Given the absence of XMLD contrast and the fragile magnetic response observed even in structurally well-ordered films, we infer that magnetic coupling in sputtered MBT is highly sensitive to subtle disorder. This fragility may originate from residual Mn intercalation or stacking faults that disrupt the van der Waals layer coupling, as well as from kinetic segregation during annealing, whereby excess Mn or Te phase-separates and stabilizes competing configurations. Additionally, the independent Te flux introduced during growth, absent in previous MBE doping studies, may alter the Mn bonding environment or suppress Te vacancies, shifting the balance between magnetic phases. Further improvements may be achieved by optimizing the post-deposition annealing protocol, which is central to crystallization in sputtered films. Since deposition occurs at room temperature, excess Mn may segregate during the anneal, particularly if the Te flux stabilizes competing $MnTe_x$-type configurations. Slower ramp rates or multistage annealing may improve Mn incorporation and reduce intercalation or clustering. Additionally, more precise in situ control of relative fluxes could help maintain the narrow stoichiometric window required for MBT stability. Finally, the use of alternative substrates with better lattice match or van der Waals character may reduce interfacial strain and promote coherent septuple-layer stacking.

3. Conclusions

We have investigated the structural and magnetic properties of MBT thin films synthesized by magnetron sputtering under varying stoichiometric conditions. While this growth method offers a promising route to scalable, smooth, and compositionally tunable magnetic TI films, significant challenges remain in realizing the intrinsic antiferromagnetic order required for accessing exotic quantum phases such as the QAHE and the axion insulator state.[15,24,26] Our results show that while nominally stoichiometric films exhibit improved structural characteristics, such as lower roughness, reduced twinning, and more defined diffraction signatures, this morphological improvement does not straightforwardly translate into long-range magnetic order. SQUID magnetometry and XMCD reveal that both stoichiometric and Mn-rich films host sizable Mn magnetic moments, but only weak signatures of antiferromagnetic transitions are observed, and no reliable XMLD signal could be extracted. These findings are consistent with previous reports highlighting the sensitivity of MBT magnetism to structural disorder, Mn intercalation, and deviations from desired stoichiometry.[20,21,34] The absence of a robust XMLD signal, even in smooth films, suggests that the anticipated odd–even layer effects, clearly visible in exfoliated bulk samples,[26] may be suppressed by local magnetic inhomogeneity, stacking faults, or incomplete formation of the MBT septuple layer structure during sputtering. These effects could also contribute to partial decoupling of Mn sublattices, disrupting the A-type antiferromagnetic configuration.[19,27]

Future efforts should focus on a more detailed microscopic analysis of sputtered films using high-resolution transmission electron microscopy and X-ray photoelectron spectroscopy to directly assess phase purity, interface quality, and local stoichiometry. In parallel, refining the post-deposition annealing process and exploring alternative substrate materials may help reduce lattice strain and enhance interlayer magnetic coupling. The implementation of optimized capping layers to suppress Te desorption during annealing could further improve the structural and magnetic uniformity of MBT films. These steps will be essential to fully evaluate whether sputtering can serve as a viable alternative to exfoliation-based approaches for stabilizing antiferromagnetic topological order in MBT. Overall, while the realization of intrinsic magnetic topological behavior in sputtered MBT films remains elusive, our study provides important insight into the interplay between growth conditions, structural morphology, and magnetic response. This work helps to narrow down the experimental parameter space to be probed and highlights the need for further refinement of growth protocols in the search for scalable platforms that exhibit the full range of quantum effects predicted for magnetic TIs.

4. Experimental Section

MBT thin films were deposited on $10 \times 10\,mm^2$ Al_2O_3 (0001) substrates. The 430-μm-thick substrates were cleaned sequentially in acetone, isopropanol, and deionized water using an ultrasonic bath. Film growth was carried out in a magnetron sputtering system with a base pressure of 2×10^{-8} mbar. Cosputtering was performed at room temperature using 2″ targets of Bi_2Te_3 (99.999% purity), Mn (99.9%), and Te (99.9%) under an Ar atmosphere at a working pressure of 1.2×10^{-2} mbar. The Al (99.9%) target was used post-growth to deposit a protective capping layer. The deposition rates of the individual targets were determined ex situ using X-ray reflectivity (XRR) measurements on single-element calibration films grown under identical sputtering conditions. The resulting rates were ≈0.00612 nm/s/W for Bi_2Te_3 (0.122 nm s^{-1} at 20 W), 0.00357 nm/s/W for Te (0.0179–0.0286 nm s^{-1} at 5–8 W), and 0.00598 nm/s/W for Mn (0.0239–0.0598 nm s^{-1} at 4–10 W), with some variability due to chamber conditions and target aging.

Following deposition, the samples were annealed in situ at 375 °C for 3 h to promote crystallization. Once cooled, a 3–4 nm-thick Al layer was sputtered onto the film surface to protect against ambient oxidation, yet allowing for soft X-ray spectroscopy. A series of films was fabricated with varying relative sputter powers to identify conditions that yield near-stoichiometric MBT, evaluated through structural and compositional characterization.

XRD measurements were conducted in multiple geometries to probe the crystallographic quality and texture. Symmetric θ–2θ scans were used to assess out-of-plane orientation. Note that a K^{β} filter was used to remove additional peaks, notably distorting the substrate peaks. Reciprocal space mapping (RSM) in asymmetric geometry was performed to access reflections outside of the *c*-axis and to distinguish between MBT and Bi_2Te_3 phases, which exhibit nearly overlapping (003*l*) peaks in symmetric geometry. The angle χ represents a rotation of the sample about the axis parallel to the incident X-ray beam, enabling access to out-of-plane and tilted lattice planes. This geometry effectively produces a 2D reciprocal space section. To evaluate in-plane ordering and rotational domain structure, azimuthal (φ) scans were performed on selected asymmetric peaks to detect twinning, a common defect in hexagonal-layered materials that results in 60° in-plane rotations of the unit cell.

AFM was used in tapping mode to assess surface morphology and roughness and to estimate grain size. Variations in microstructure and roughness were correlated with composition and phase evolution derived from XRD.

Magnetic characterization was performed using a SQUID-VSM to measure both field-dependent and temperature-dependent magnetization. These measurements were used to identify characteristic magnetic transitions, assess hysteresis behavior, and guide the interpretation of synchrotron-based spectroscopy. Both out-of-plane and in-plane magnetization curves were recorded to assess anisotropy and magnetic ordering symmetry. To isolate the weak magnetic signal from the film, the diamagnetic background of a bare sapphire substrate from the same batch was measured under identical mounting conditions (straw) and subtracted from the raw data.

Element-specific magnetic information was obtained using X-ray magnetic dichroism techniques at the Mn $L_{2,3}$ absorption edges. Experiments were conducted at the I10 (BLADE) beamline at Diamond Light Source (Didcot, UK) and the BOREAS beamline BL29 at ALBA Synchrotron (Barcelona, Spain). Measurements were carried out at base temperatures of ≈2 K in magnetic fields up to 14 T applied parallel to the beam direction.

XAS using circularly polarized X-rays was recorded in total electron yield (TEY) mode to probe surface-sensitive magnetic moments, with an estimated probing depth of 3–5 nm.[49] To assess whether surface-sensitive data reflected bulk-like behavior, selected measurements were also performed in luminescence yield (LY) mode, which gives a measure for the X-ray absorption of the sample along its entire thickness. In this method, the X-rays that are transmitted through the sample are detected by the X-ray excited optical luminescence (XEOL) in the substrate, where the created optical photons are captured by a photodiode behind the sample. LY provides complementary information where TEY data may be limited by surface oxidation.

XMCD was used to extract qualitative and semi-quantitative information on magnetic moment magnitude and orientation. Measurements under both polarizations were normalized to incident beam intensity and corrected for linear background. Where applicable, sum rules analysis was used to estimate spin and orbital moments.[39] Attempts to detect XMLD signatures of antiferromagnetic order were also made; however, no reproducible signal was observed, likely due to residual roughness and magnetic disorder.

Acknowledgements

The XMCD experiments were carried out on beamline I10 at the Diamond Light Source under proposal MM36644 and on beamline BL29 BOREAS at ALBA under proposal 22023097783. Financial support from the Leverhulme Trust (RPG-2020-358), the John Fell Fund (University of Oxford), the Oxford-ShanghaiTech collaboration project, and the UK Skyrmion Project (Engineering and Physical Sciences Research Council, EP/N032128/1) is acknowledged. J.B. was supported by the Leverhulme Trust, E.H. acknowledges an STFC-Diamond-EPSRC studentship (grant nos. 2604894, EP/R513295/1, and EP/T517811/1), and J.B. and E.L.A. Diamond-EPSRC studentships (grant nos. 2606404, EP/R513295/1, EP/T517811/1, and EP/W524311/1).

Conflict of Interest

The authors declare no conflict of interest.

Author Contributions

Joshua Bibby: data curation (lead); formal analysis (lead); investigation (lead); methodology (equal); software (equal); validation (equal); visualization (lead); writing—original draft (lead). **Emily Heppell**: data curation (equal); methodology (supporting). **Jack Bollard**: data curation (supporting). **Ethan L. Arnold**: data curation (supporting). **Javier Herrero-Martín**: data curation (equal); methodology (equal); software (lead). **Gerrit van der Laan**: conceptualization (lead); data curation (equal); formal analysis (equal); funding acquisition (supporting); investigation (equal); methodology (lead); project administration (supporting); resources (lead); software (supporting); supervision (equal); validation (lead); writing—review and editing (equal). **Thorsten Hesjedal**: conceptualization (lead); data curation (supporting); funding acquisition (lead); investigation (supporting); methodology (lead); project administration (lead); resources (lead); supervision (lead); validation (supporting); visualization (supporting); writing—original draft (equal); writing—review and editing (lead).

Data Availability Statement

The data that support the findings of this study are available from the corresponding author upon reasonable request.

Keywords

magnetic topological insulators, magnetron sputtering, $MnBi_2Te_4$, thin film growth, X-ray magnetic circular dichroism

Received: August 12, 2025
Published online:

[1] M. Z. Hasan, C. L. Kane, *Rev. Mod. Phys.* **2010**, *82*, 3045.
[2] X.-L. Qi, S.-C. Zhang, *Rev. Mod. Phys.* **2011**, *83*, 1057.
[3] Y. Tokura, K. Yasuda, A. Tsukazaki, *Nat. Rev. Phys.* **2019**, *1*, 126.

[4] A.-M. Netsou, D. A. Muzychenko, H. Dausy, T. Chen, F. Song, K. Schouteden, M. J. van Bael, C. van Haesendonck, *ACS Nano* **2020**, *14*, 13172.
[5] Y. Xia, D. Qian, D. Hsieh, L. Wray, A. Pal, H. Lin, A. Bansil, D. Grauer, Y. S. Hor, R. J. Cava, M. Z. Hasan, *Nat. Phys.* **2009**, *5*, 398.
[6] G. Wang, X.-G. Zhu, Y.-Y. Sun, Y.-Y. Li, T. Zhang, J. Wen, X. Chen, K. He, L.-L. Wang, X.-C. Ma, J.-F. Jia, S. B. Zhang, Q.-K. Xue, *Adv. Mater.* **2011**, *23*, 2929.
[7] J. G. Analytis, J.-H. Chu, Y. Chen, F. Corredor, R. D. McDonald, Z. X. Shen, I. R. Fisher, *Phys. Rev. B* **2010**, *81*, 205407.
[8] D. Kong, Y. Chen, J. J. Cha, Q. Zhang, J. G. Analytis, K. Lai, Z. Liu, S. S. Hong, K. J. Koski, S.-K. Mo, Z. Hussain, I. R. Fisher, Z.-X. Shen, Y. Cui, *Nat. Nanotechnol.* **2011**, *6*, 705.
[9] D.-X. Qu, Y. S. Hor, J. Xiong, R. J. Cava, N. P. Ong, *Science* **2010**, *329*, 821.
[10] J. Liu, T. Hesjedal, *Adv. Mater.* **2023**, *35*, 2102427.
[11] C.-Z. Chang, J. Zhang, X. Feng, J. Shen, Z. Zhang, M. Guo, K. Li, Y. Ou, P. Wei, L.-L. Wang, Z.-Q. Ji, Y. Feng, S. Ji, X. Chen, J. Jia, X. Dai, Z. Fang, S.-C. Zhang, K. He, Y. Wang, L. Lu, X.-C. Ma, Q.-K. Xue, *Science* **2013**, *340*, 167.
[12] M. D. Watson, L. J. Collins-McIntyre, L. R. Shelford, A. I. Coldea, D. Prabhakaran, S. C. Speller, T. Mousavi, C. R. M. Grovenor, Z. Salman, S. R. Giblin, G. van der Laan, T. Hesjedal, *New J. Phys.* **2013**, *15*, 103016.
[13] J. Bibby, A. Singh, E. Heppell, J. Bollard, B. Achinuq, S. J. Haigh, G. van der Laan, T. Hesjedal, *Crystals* **2025**, *15*, 54.
[14] D. Zhang, M. Shi, T. Zhu, D. Xing, H. Zhang, J. Wang, *Phys. Rev. Lett.* **2019**, *122*, 206401.
[15] M. M. Otrokov, I. I. Klimovskikh, H. Bentmann, D. Estyunin, A. Zeugner, Z. S. Aliev, S. Gaß, A. U. B. Wolter, A. V. Koroleva, A. M. Shikin, M. Blanco-Rey, M. Hoffmann, I. P. Rusinov, A. Y. Vyazovskaya, S. V. Eremeev, Y. M. Koroteev, V. M. Kuznetsov, F. Freyse, J. Sanchez-Barriga, I. R. Amiraslanov, M. B. Babanly, N. T. Mamedov, N. A. Abdullayev, V. N. Zverev, A. Alfonsov, V. Kataev, B. Büchner, E. F. Schwier, S. Kumar, A. Kimura, et al., *Nature* **2019**, *576*, 416.
[16] J. Li, Y. Li, S. Du, Z. Wang, B.-L. Gu, S.-C. Zhang, K. He, W. Duan, Y. Xu, *Sci. Adv.* **2019**, *5*, eaaw5685.
[17] S. Li, T. Liu, C. Liu, Y. Wang, H.-Z. Lu, X. C. Xie, *Natl. Sci. Rev.* **2023**, *11*, nwac296.
[18] C. Lei, A. H. MacDonald, Kerr, Faraday, *Phys. Rev. B* **2023**, *108*, 125424.
[19] Q. Li, S.-K. Mo, M. T. Edmonds, *Nanoscale* **2024**, *16*, 14247.
[20] A. Y. Vyazovskaya, M. Bosnar, E. V. Chulkov, M. M. Otrokov, *Mater.* **2025**, *6*, 88.
[21] A. Zeugner, F. Nietschke, A. U. B. Wolter, S. Gaß, R. C. Vidal, T. R. F. Peixoto, D. Pohl, C. Damm, A. Lubk, R. Hentrich, S. K. Moser, C. Fornari, C. H. Min, S. Schatz, K. Kißner, M. Ünzelmann, M. Kaiser, F. Scaravaggi, B. Rellinghaus, K. Nielsch, C. Hess, B. Büchner, F. Reinert, H. Bentmann, O. Oeckler, T. Doert, M. Ruck, A. Isaeva, *Chem. Mater.* **2019**, *31*, 2795.
[22] D. Zhang, M. Shi, T. Zhu, D. Xing, H. Zhang, J. Wang, *Phys. Rev. Lett.* **2019**, *122*, 206401.
[23] P. Wang, J. Ge, J. Li, Y. Liu, Y. Xu, J. Wang, *The Innovation* **2021**, *2*, 100098.
[24] Y. Bai, Y. Li, J. Luan, R. Liu, W. Song, Y. Chen, P.-F. Ji, Q. Zhang, F. Meng, B. Tong, L. Li, Y. Jiang, Z. Gao, L. Gu, J. Zhang, Y. Wang, Q.-K. Xue, K. He, Y. Feng, X. Feng, *Natl. Sci. Rev.* **2023**, *11*, nwad189.
[25] Y. Shi, Y. Bai, Y. Li, Y. Feng, Q. Li, H. Zhang, Y. Chen, Y. Tong, J. Luan, R. Liu, P. Ji, Z. Gao, H. Guo, J. Zhang, Y. Wang, X. Feng, K. He, X. Zhou, J. Shen, *Phys. Rev. Mater.* **2024**, *8*, 124202.
[26] S. Li, M. Gong, S. Cheng, H. Jiang, X. C. Xie, *Natl. Sci. Rev.* **2023**, *11*, nwad262.
[27] T. Jansen, E. Kochetkova, A. Isaeva, A. Brinkman, C. Li, *Mater.* **2024**, *5*, 214.
[28] T. Fukasawa, S. Kusaka, K. Sumida, M. Hashizume, S. Ichinokura, Y. Takeda, S. Ideta, K. Tanaka, R. Shimizu, T. Hitosugi, T. Hirahara, *Phys. Rev. B* **2021**, *103*, 205405.
[29] P. Kagerer, C. I. Fornari, S. Buchberger, S. L. Morelhão, R. C. Vidal, A. Tcakaev, V. Zabolotnyy, E. Weschke, V. Hinkov, M. Kamp, B. Büchner, A. Isaeva, H. Bentmann, F. Reinert, *J. Appl. Phys.* **2020**, *128*, 135303.
[30] T. Zhu, A. J. Bishop, T. Zhou, M. Zhu, D. J. O'Hara, A. A. Baker, S. Cheng, R. C. Walko, J. J. Repicky, T. Liu, J. A. Gupta, C. M. Jozwiak, E. Rotenberg, J. Hwang, *Nano Lett.* **2021**, *21*, 5083.
[31] A. M. Shikin, D. A. Estyunin, I. I. Klimovskikh, S. O. Filnov, E. F. Schwier, S. Kumar, K. Miyamoto, T. Okuda, A. Kimura, K. Kuroda, K. Yaji, S. Shin, Y. Takeda, Y. Saitoh, Z. S. Aliev, N. T. Mamedov, I. R. Amiraslanov, M. B. Babanly, M. M. Otrokov, S. V. Eremeev, E. V. Chulkov, *Sci. Rep.* **2020**, *10*, 13226.
[32] X. Yao, Q. Cui, Z. Huang, X. Yuan, H. T. Yi, D. Jain, K. Kisslinger, M.-G. Han, W. Wu, H. Yang, S. Oh, *Nano Lett.* **2024**, *24*, 9923.
[33] J. Sun, S. Liu, F. Xiu, W. Liu, *2024 IEEE Inter. Magnetic Conf. - Short papers (INTERMAG Short papers)*, IEEE, Rio de Janeiro, Brazil **2024**, 1–2.
[34] J. Sitnicka, K. Park, P. Skupiński, K. Grasza, A. Reszka, K. Sobczak, J. Borysiuk, Z. Adamus, M. Tokarczyk, A. Avdonin, I. Fedorchenko, I. Abaloszewa, S. Turczyniak-Surdacka, N. Olszowska, J. Kolodziej, B. J. Kowalski, H. Deng, M. Konczykowski, L. Krusin-Elbaum, A. Wolos, *2D Mater.* **2021**, *9*, 15026.
[35] H. Lu, Y. Huang, Q. Guo, K. Wang, M. He, Z. Yin, D. Wang, T. Liu, J. Wang, G. Yu, J. Teng, *J. Phys. D: Appl. Phys.* **2023**, *56*, 045302.
[36] J. Kampmeier, S. Borisova, L. Plucinski, M. Luysberg, G. Mussler, D. Grützmacher, *Cryst. Growth Des.* **2015**, *15*, 390.
[37] L. J. Collins-McIntyre, S. E. Harrison, P. Schönherr, N.-J. Steinke, C. J. Kinane, T. R. Charlton, D. Alba-Veneroa, A. Pushp, A. J. Kellock, S. S. P. Parkin, J. S. Harris, S. Langridge, G. van der Laan, T. Hesjedal, *Europhys. Lett.* **2014**, *107*, 57009.
[38] Y. H. Choi, N. H. Jo, K. J. Lee, H. W. Lee, Y. H. Jo, J. Kajino, T. Takabatake, K.-T. Ko, J.-H. Park, M. H. Jung, *Appl. Phys. Lett.* **2012**, *101*, 152103.
[39] B. T. Thole, P. Carra, F. Sette, G. van der Laan, *Phys. Rev. Lett.* **1992**, *68*, 1943.
[40] J.-Q. Yan, Q. Zhang, T. Heitmann, Z. Huang, K. Y. Chen, J.-G. Cheng, W. Wu, D. Vaknin, B. C. Sales, R. J. McQueeney, *Phys. Rev. Mater.* **2019**, *3*, 064202.
[41] H. Tan, B. Yan, *Phys. Rev. Lett.* **2023**, *130*, 126702.
[42] X. Wu, C. Ruan, P. Tang, F. Kang, W. Duan, J. Li, *Nano Lett.* **2023**, *23*, 5048.
[43] C. Bigi, L. Qiao, C. Liu, P. Barone, M. C. Hatnean, G.-R. Siemann, B. Achinuq, D. A. Mayoh, G. Vinai, V. Polewczyk, D. Dagur, F. Mazzola, P. Bencok, T. Hesjedal, G. van der Laan, W. Ren, G. Balakrishnan, S. Picozzi, P. D. C. King, *Phys. Rev. B* **2023**, *108*, 054419.
[44] E. L. Arnold, J. M. Riley, L. B. Duffy, A. I. Figueroa, R. Held, K. M. Shen, D. G. Schlom, P. D. C. King, M. Hoesch, G. van der Laan, T. Hesjedal, *Phys. Rev. Mater.* **2025**, *9*, 024410.
[45] S. K. Sharma, H. R. Prakash, S. Ram, D. Pradhan, *AIP Conf. Proc.* **2018**, *1942*, 130044.
[46] B. A. Jensen, W. Tang, X. Liu, A. I. Nolte, G. Ouyang, K. W. Dennis, J. Cui, *Acta Mater.* **2019**, *181*, 595.
[47] K. Vero, J. P. Borah, *Sci. Rep.* **2024**, *14*, 19015.
[48] S.-Y. Xu, M. Neupane, C. Liu, D. Zhang, A. Richardella, L. A. Wray, N. Alidoust, M. Leandersson, T. Balasubramanian, J. Sánchez-Barriga, O. Rader, G. Landolt, B. Slomski, J. H. Dil, J. Osterwalder, T.-R. Chang, H.-T. Jeng, H. Lin, A. Bansil, N. Samarth, M. Z. Hasan, *Nat. Phys.* **2012**, *8*, 616.
[49] G. van der Laan, A. I. Figueroa, *Coord. Chem. Rev.* **2014**, *277–278*, 95.